

Composite structures, DOI link:

<https://doi.org/10.1016/j.compstruct.2021.114745>

Assessment of the 3D ply-by-ply fiber structure in impacted CFRP by means of planar Ultrasound Computed Tomography (pU-CT)

Xiaoyu Yang^{a,b,*} Bing-feng Ju^b and Mathias Kersemans^{a,*}

^a*Mechanics of Materials and Structures (UGent-MMS), Ghent University, Ghent, Belgium*

^b*The State Key Laboratory of Fluid Power Transmission and Control, Zhejiang University, Hangzhou, People's Republic of China*

ARTICLE INFO

Keywords:

fiber-reinforced polymer
impact damage
ultrasonic pulse-echo
technique
analytic-signal technology
planar ultrasound computed
tomography
fiber architecture

ABSTRACT

The manufacturing process of fiber reinforced polymer laminates could induce local distortions from the nominal fiber architecture. Further, low-velocity impact events may induce additional changes in the fiber architecture, due to local plasticity and delamination formation. These deviations could have a significant effect on the structural performance of the composite laminate.

This study presents a planar ultrasound computed tomography (pU-CT) technique to reconstruct the local fiber architecture of impacted carbon fiber reinforced polymer laminates. The proposed pU-CT technique employs a pulse-echo scanning modality, and the 3D reconstruction process consists of three subsequent analysis steps:

- Step 1: Extraction of front- and rear surfaces, delamination interfaces, and interply interfaces by a hybrid analytic-signal analysis.
- Step 2: Estimation of the out-of-plane ply orientation using a structure tensor process.
- Step 3: Extraction of the in-plane fiber direction by means of a Gabor filter-based information diagram.

The developed pU-CT technique is experimentally demonstrated on an impacted 24-layer CFRP laminate with a stacking sequence $[45/0/-45/90]_{3S}$. The obtained 3D reconstruction result reveals that the impact event introduced a complex delamination cluster, as well as local plasticity resulting in distorted out-of-plane ply orientation. The in-plane fiber angles remain unaffected and closely match the nominal quasi-isotropic stacking sequence.

It is anticipated that the pU-CT method could complement X-ray computed tomography measurements, especially for the inspection of (damaged) CFRP laminates with sizeable dimensions.

1. Introduction

Carbon fiber reinforced polymers (CFRP), or composites, have broad applications in construction, aerospace, automotive, and wind power industries thanks to their good structural performance [1]. They rely on the aligned carbon fibers and the cohesive matrix that holds the fibers together to gain superior specific strength and stiffness. Furthermore, by optimal design of the stacking sequence and fiber orientation, one can tailor the mechanical properties and performance to certain applications. Nowadays, manual manufacturing methods are still employed, which could induce errors in the lay-up. Furthermore, for autoclave-based processes, the varying quality in prepreg (uncured single ply) might lead to small local distortions of the intended fiber architecture [2]. Hence, in order to assure the manufacturing quality and as such the structural performance, it is necessary to evaluate the fiber architecture in a non-destructive manner.

Apart from the manufacturing process, distortions could also arise during the operational lifetime of the composite. Low-velocity impact (LVI) events are well-known to pose a severe threat to structural integrity [3]. LVI typically induces barely visible impact damage (BVID) which is a complex damage phenomenon that consists of fiber breakage, delaminations, matrix cracking, and plastic deformations [4, 5]. Hence, such an impact event can locally alter the fiber architecture significantly, and as such may greatly reduce the structural performance of the composite. Of particular concern is that the BVID can rarely be detected by visual inspection and might grow upon further loading [6]. For example, a highly reduced compression-after-impact strength has been reported in the literature [7, 8]. The reduction in strength is mainly attributed to the presence of delaminations, promoted by matrix cracks, stiffness mismatch, ply clustering, and the laminate deflection [9], as well as to the out-of-plane plastic deformation coming along with local buckling [10]. Thus, considerable research attention is drawn to the evaluation of the BVID in composites in order to prevent structures from sudden catastrophic failure. For this purpose, various non-destructive testing (NDT) methods are being developed, such as X-ray computed tomography (X-CT) [11-17], ultrasonic testing (UT) [18-27], infrared thermography [28-32], and eddy current testing [33-35].

X-CT is feasible in investigating the behavior and damage of composite materials undergoing impact loading, through which considerable details can be provided to assess the internal structure within the material structure [12, 13, 15]. The dataset obtained from X-CT analysis provides rich information on the material structure and internal shape [11]. In recent progress, a voxel-based description of the representative volume element has been automatically generated by applying the structural tensor process to the micro-CT images [16]. On merit with this quantitative analysis, realistic modeling of composite materials is derived from the CT images for knowledge of the orientations of the fibers and the local (anisotropic) properties [16, 17]. The major concerns with X-CT are however the harmful radiation, the high experimental time, the limited contrast for CFRP composites, and the limitation of the sample size [13, 15].

Several UT techniques have been developed for NDT of composite structures. Ultrasound shows high sensitivity to various damage types typically found in composites [22, 27]. However, UT normally provides low signal-to-noise ratio (SNR) signals or low-contrast images due to high attenuation, wave diffraction, and complicated reflections in composites [24, 36]. This makes the quantitative evaluation of the fiber architecture challenging [23], and requires advanced signal or image processing algorithms. In this regard, the application of the analytic-signal technique coupled with different advanced analysis tools was successful in extracting information on the local fiber architecture. Especially when coupled to an ultrasonic input signal with frequency content close to the ply-resonance frequency, promising results were obtained. The instantaneous amplitude is evaluated to determine the surfaces and delaminations associated with the strong echoes induced by the front-surface (water-to-composite interface), rear-surface (composite-to-water interface), and delamination (composite-to-air interface) [37]. The interplies (ply-to-ply interface) rather induce weak echoes. However, the echoes from the interplies are characterized by an instantaneous phase of $\phi_0 - \pi/2$, where ϕ_0 is the phase of the input pulse [37]. As such, the interplies can be determined by the evaluation of the instantaneous phase. Recently, the current authors proposed the additional use of a log-Gabor filter in order to obtain optimal scale selection in the ultrasonic response signal. This resulted in an improved noise-filtering as well as a more robust interply determination [38, 39]. Extraction of the in-plane fiber orientation of a composite laminate has also been done by means of the Radon transform [40]. In [41, 42], researchers have demonstrated the quantification of out-of-plane fiber wrinkling by means of a structure tensor process.

This study proposes a planar ultrasound computed tomography (pU-CT) technique, for reconstructing the local ply-fiber architecture of impacted CFRP laminates. The proposed pU-CT consists of three steps. The first step is a hybrid analytic-signal analysis to determine the surfaces, the interplies, and the delaminations in a robust and efficient manner. Step 2 makes use of a structure tensor process for the extraction of the local out-of-plane ply orientation. In step 3, a Gabor

filter-based Information Diagram (GF-ID) method is employed for the robust extraction of the local in-plane fiber direction. The developed pU-CT technique is demonstrated on a 24-layer quasi-isotropic CFRP laminate which suffered an LVI event with an energy of 5.3 J.

This paper is organized as follows. The novel pU-CT technique is introduced in section 2. The impacted CFRP laminate and the experimental methodology are described in section 3. The obtained results and discussions are given in section 4. Finally, the conclusion is presented in section 5.

2. Planar Ultrasound Computed Tomography pU-CT methodology

The underlying assumption made in the pU-CT approach is that the excitation signal is sufficiently broadband such that both the fundamental ply-resonance and the 2nd-harmonic ply-resonance are excited with sufficient energy. The pU-CT method consists of three steps, and each step extracts a specific metric from the structure of the composite (see Figure 1). The three steps are detailed in the following subsections.

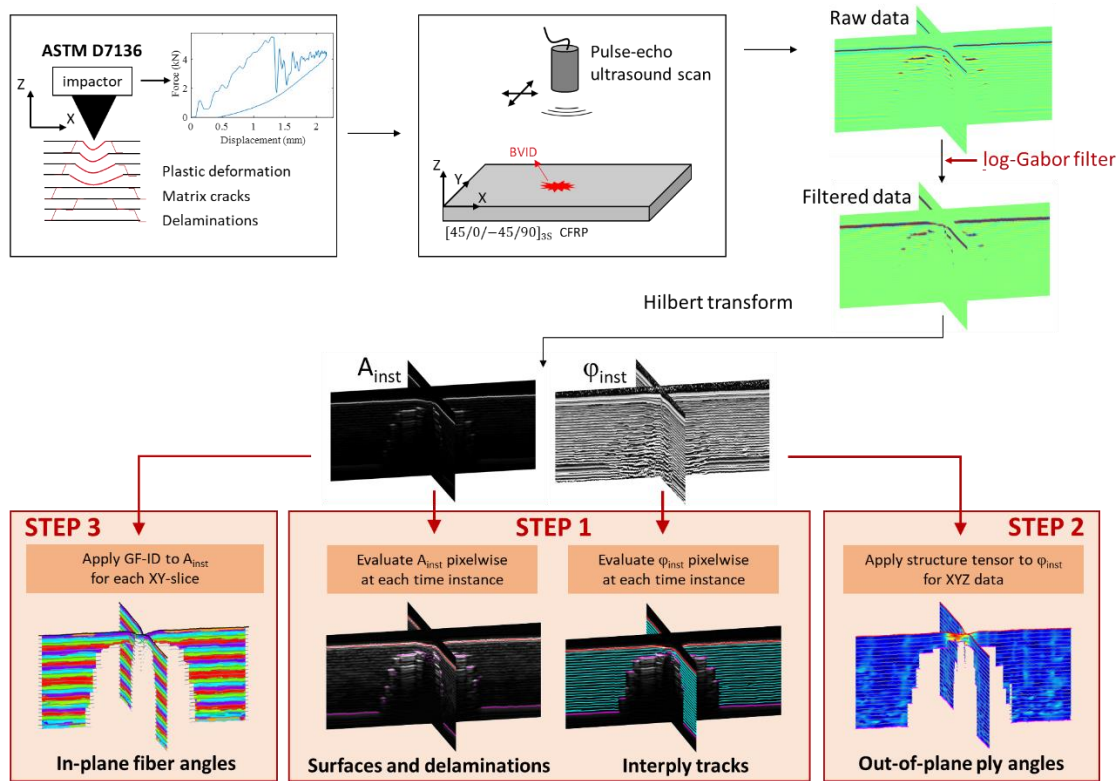


Figure 1: Conceptual overview of the pU-CT method.

2.1. Step 1: Interface mapping via hybrid analytic-signal analysis

A hybrid analytic-signal analysis is employed in order to distinguish between the ultrasonic reflections from different interfaces, i.e., front- and rear surfaces, delaminations, and resin-rich interplies between CFRP plies. The analytic-signal is composed of a real part $s(t)$, which corresponds to the recorded signal, and an imaginary part $g(t)$:

$$s_a(t) = s(t) + ig(t), \quad (1)$$

with $g(t)$ the Hilbert transform of $s(t)$ according to

$$g(t) = \int_{-\infty}^{+\infty} \frac{s(\tau)}{\pi(t-\tau)} d\tau \quad (2)$$

In the frequency domain, the relationship between a recorded signal and its analytic-signal can be rewritten as

$$F_a(\omega) = (1 + \text{sgn}(\omega))F(\omega), \quad (3)$$

where $F_a(\omega)$ is the Fourier spectrum of $s_a(t)$, $F(\omega)$ is the Fourier spectrum of $s(t)$, ω is the angular frequency, and $\text{sgn}(\cdot)$ denotes the sign function. The log-Gabor filter to decompose the signal in different scales is defined as follows:

$$G(\omega) = \exp\left(\frac{-(\log\frac{|\omega|}{2\pi f_0})^2}{2(\log\sigma_0)^2}\right), \quad (4)$$

where f_0 and σ_0 govern the center frequency and bandwidth of the passband respectively. The filtered spectrum $\tilde{F}_a(\omega)$ is obtained by multiplication of $F_a(\omega)$ with $G(\omega)$:

$$\tilde{F}_a(\omega) = G(\omega)F_a(\omega). \quad (5)$$

The filtered analytic-signal in the time domain is obtained by the application of an inverse Fourier transform:

$$\tilde{s}_a(t) = IFT\left(\tilde{F}_a(\omega)\right), \quad (6)$$

where $IFT(\cdot)$ denotes the inverse Fourier transform. Finally, the instantaneous amplitude $A_{inst}(t)$ and instantaneous phase $\phi_{inst}(t)$ can be derived as follows:

$$A_{inst}(t) = \sqrt{[Re(\tilde{s}_a(t))]^2 + [Im(\tilde{s}_a(t))]^2}, \quad (7)$$

$$\phi_{inst}(t) = \arctan\left(\frac{Im(\tilde{s}_a(t))}{Re(\tilde{s}_a(t))}\right) + \pi \times \text{sgn}(Im(\tilde{s}_a(t))). \quad (8)$$

The instantaneous amplitude is first evaluated to derive the time-of-flight (TOF) of the front-wall, back-wall, and delamination echoes (see Figure 2). The first peak amplitude exceeding typical magnitudes is defined as the front-wall echo. In order to determine the delamination and back-wall echoes appropriately, a dynamic amplitude correction is performed for compensating the ultrasonic attenuation through depth. Here, the echo with an amplitude A_b exceeding the dynamic reference amplitude is determined as the echo corresponding to the back-wall or delamination as follows:

$$A_b > 0.5A_f \times \exp\left(-\alpha_{DAC}(TOF_b - TOF_f)\right), \quad (9)$$

where A_f and TOF_f are the amplitude and the TOF of the front-wall echo respectively, TOF_b is the TOF of the echo A_b (which can correspond to a delamination echo or the back-wall echo), and α_{DAC} is a compensation factor set as $0.75 / \mu\text{s}$. This specific value is chosen based on the amplitude and TOF of both the front- and back-wall echoes.

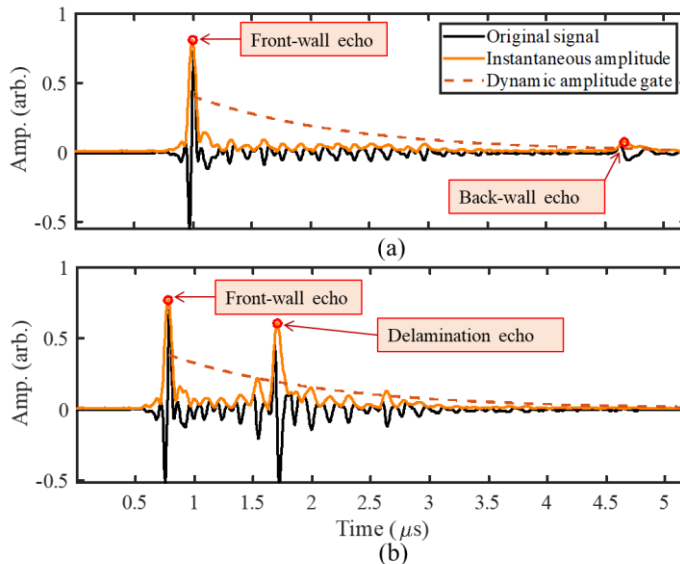


Figure 2: (a) Healthy and (b) delaminated A-scan signals from the impacted CFRP laminate with indication of the

dynamic amplitude gate.

The instantaneous phase associated with the front-wall echo is set to ϕ_0 , and the instantaneous phase at the fundamental ply-resonance is used for the basic interply tracking [37]. The interply track represents the location of the resin-rich layer between adjacent CFRP plies. Practically, the interpolated $\phi_0 - \pi/2$ position in each 2π phase cycle is tracked, and the corresponding TOF indicates the depth positions of the interplies. Though, the dominating nature of the front-wall, back-wall and delamination echoes makes the extraction of nearby interplies problematic [37-39]. In order to reduce this dominating effect, the instantaneous phase at the 2nd-harmonic ply-resonance is analyzed to derive these nearby interplies (see Figure 3b). Practically, the interpolated $\phi_0 - \pi/2$ positions in the second and the second-to-last 2π phase cycles are tracked, and the corresponding TOF indicate the depth positions of the first and the last interplies. Hence, we analyze the instantaneous phase at fundamental ply-resonance for stable interply tracking, and take advantage of the 2nd-harmonic ply-resonance to reduce the dominating effect of the wall echoes (see Figure 3b and c). To obtain specific ply-resonance frequencies for this hybrid instantaneous phase analysis, two log-Gabor filters are applied to optimally decompose the ultrasonic reflection signal. This improved analysis however requires that the input signal is sufficiently broadband such that the decomposition can be done in a stable and robust manner.

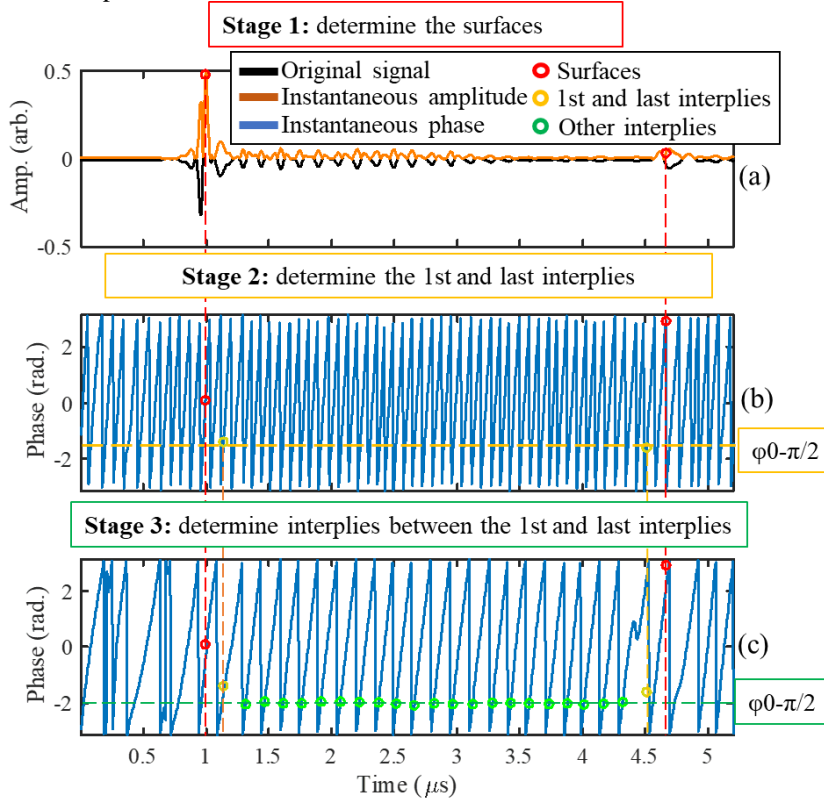


Figure 3: Illustration of the hybrid analytic-signal analysis on a healthy A-scan signal: (a) Extraction of surface echoes by the instantaneous amplitude of the original signal, (b) extraction of the first and the last interplies using the instantaneous phase of the filtered signal at the 2nd-harmonic ply-resonance, and (c) extraction of other interplies using the instantaneous phase of the filtered signal at the fundamental ply-resonance.

2.2. Step 2: Out-of-plane ply angle via structure tensor process

The structure tensor process is a flexible and robust method for determining structure orientations in a smoothly varying field [43]. In this study, the structure tensor process is applied to the instantaneous phase of the filtered signal at the 2nd-harmonic ply-resonance (obtained in section 2.1). For the function $\phi_{inst}(x, y, t)$, the structure tensor is defined as

$$S_G(p) = \int G_\tau(r) S_0(p - r) dr, \quad (10)$$

with $p = (x, y, t)$ and $r \in R^3$. $G_\tau(r)$ is a 3D Gaussian smoothing kernel according to

$$G_\tau(r) = \frac{1}{(\sqrt{2\pi}\tau)^3} \exp\left(-\frac{|r|^2}{2\tau^2}\right) \quad (11)$$

With $\tau = 3$. $S_0(p)$ corresponds to

$$S_0(p) = \begin{bmatrix} (\phi_x(p))^2 & \phi_x(p)\phi_y(p) & \phi_x(p)\phi_t(p) \\ \phi_x(p)\phi_y(p) & (\phi_y(p))^2 & \phi_y(p)\phi_t(p) \\ \phi_x(p)\phi_t(p) & \phi_y(p)\phi_t(p) & (\phi_t(p))^2 \end{bmatrix}, \quad (12)$$

with $\phi_x(p)$, $\phi_y(p)$, $\phi_t(p)$ representing the three partial derivatives of $\phi_{inst}(x, y, t)$. The phase gradients are obtained by applying a central-difference kernel to the trigonometric functions as follows [42]

$$\phi_x(p) = \cos\phi_{inst}(p) \frac{\partial \sin\phi_{inst}(p)}{\partial x} - \sin\phi_{inst}(p) \frac{\partial \cos\phi_{inst}(p)}{\partial x}, \quad (13)$$

$$\phi_y(p) = \cos\phi_{inst}(p) \frac{\partial \sin\phi_{inst}(p)}{\partial y} - \sin\phi_{inst}(p) \frac{\partial \cos\phi_{inst}(p)}{\partial y}, \quad (14)$$

$$\phi_t(p) = \cos\phi_{inst}(p) \frac{\partial \sin\phi_{inst}(p)}{\partial t} - \sin\phi_{inst}(p) \frac{\partial \cos\phi_{inst}(p)}{\partial t}. \quad (15)$$

The instantaneous phase dataset is smoothed by an additional 3D Gaussian kernel G_σ before the derivation of the phase gradients. The kernels G_τ and G_σ have standard deviations of τ , and σ , respectively, which are both set as 3 in this study. Finally, the eigenvectors \mathbf{v} and eigenvalues λ_v of the tensor $S_G(p)$ are obtained which hold information about the structure's orientation at point p :

$$S_G(p)\mathbf{v} = \lambda_v\mathbf{v}, \quad (16)$$

From this, the local out-of-plane ply angle can be extracted by evaluation of the principal eigenvector as shown in Figure 4.

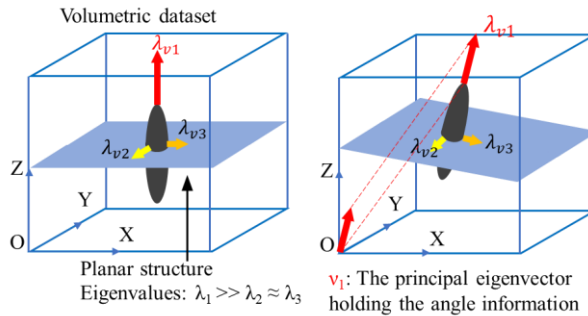


Figure 4: Illustration of extracting the principal direction of planar structures in volumetric dataset using structure tensor process.

2.3. Step 3: In-plane fiber angle via Gabor filter-based Information Diagram

The GF-ID automatically constructs a spatial 2D Gabor filter with optimal orientation and wavelength in order to estimate the local fiber direction. A 2D Gabor filter $h(x, y)$ with arbitrary orientation θ is given by [44]

$$h(x, y) = \exp\left[-\left(\frac{x'^2}{2\sigma_x^2} + \frac{y'^2}{2\sigma_y^2}\right)\right] \times \exp\left[j\left(2\pi\frac{x'}{\lambda_s} + \phi_s\right)\right], \quad (17)$$

$$x' = x\cos\theta - y\sin\theta, \quad (18)$$

$$y' = x\sin\theta + y\cos\theta, \quad (19)$$

where x and y are the spatial coordinates, λ_s and ϕ_s are the wavelength and phase of the sinusoidal plane wave along x coordinate. The parameters σ_x and σ_y determine the space constants of the Gaussian envelope along the x - and y -axes, respectively:

$$\sigma_x = \frac{\lambda_s}{\pi} \sqrt{\frac{\ln 2}{2}} \times \frac{2^{b+1}}{2^{b-1}}, \quad (20)$$

$$\sigma_y = \frac{\lambda_s}{\gamma\pi} \sqrt{\frac{\ln 2}{2}} \times \frac{2^{b+1}}{2^{b-1}}, \quad (21)$$

where b and γ are the spatial frequency bandwidth and the spatial aspect ratio respectively, which are chosen as 1 and 0.5 respectively.

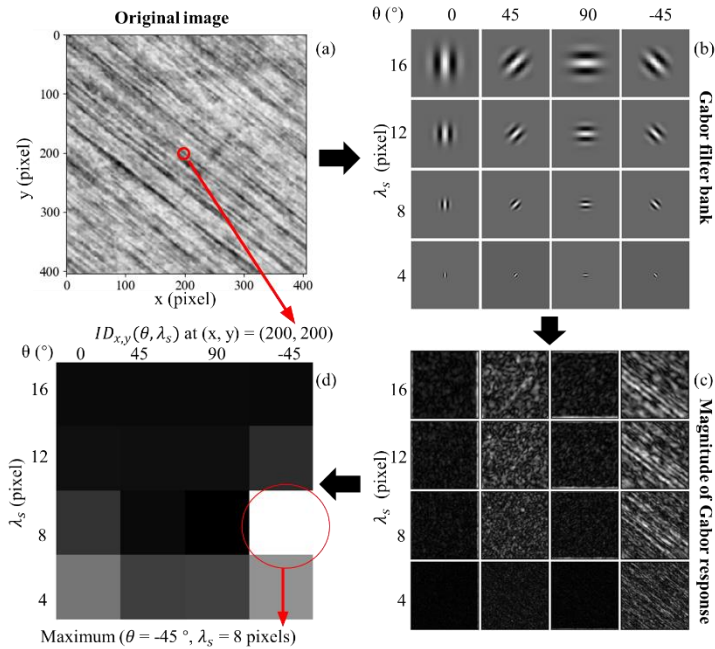


Figure 5: Illustration of the GF-ID method: (a) the original image $I(x, y)$, (b) the 2D Gabor filter bank with various wavelengths and orientations, (c) the magnitudes of the 2D Gabor filtered image, and (d) the information diagram of the pixel at location $(x, y) = (200, 200)$.

A 2D Gabor filter is applied on an image $I(x, y)$ (see Figure 5a). The normalized response $r_{\theta, \lambda_s}^n(x, y)$ is then obtained as follows [45]:

$$r_{\theta, \lambda_s}^n(x, y) = \frac{1}{2\pi\sigma_x\sigma_y} h(x, y) * I(x, y), \quad (22)$$

where $*$ denotes the convolution operator. As shown in Figure 5b, a 2D Gabor filter bank with various wavelengths and orientations is applied to $I(x, y)$. The resulting $r_{\theta, \lambda_s}^n(x, y)$ are presented in Figure 5c. An additional 2D Gaussian kernel is considered:

$$G(x, y) = \frac{2}{\pi K^2 \lambda_s^2} \exp\left(-\frac{2(x^2 + y^2)}{K^2 \lambda_s^2}\right), \quad (23)$$

where K governs the smoothness of the kernel. The K -value is selected as 2 in this study in order to reduce the sensitivity to noise.

Application of the filter kernel $G(x, y)$ to $r_{\theta, \lambda_s}^n(x, y)$ finally yields the filtered normalized response $\tilde{r}_{\theta, \lambda_s}^n(x, y)$:

$$\tilde{r}_{\theta, \lambda_s}^n(x, y) = G(x, y) * r_{\theta, \lambda_s}^n(x, y), \quad (24)$$

The magnitude of the filtered normalized response $\tilde{r}_{\theta, \lambda_s}^n(x, y)$ as a function of the 2D Gabor filter orientation and wavelength parameters forms the Information Diagram $ID_{x,y}(\theta, \lambda_s)$ (see Figure 5d). The maximum in the $ID_{x,y}(\theta, \lambda_s)$ is adopted to determine the local in-plane fiber direction at a certain pixel (x, y) .

3. Materials and methods

3.1. Material

3.1.1 Material preparation

The studied CFRP laminate consists of 24 unidirectional plies. The sample has an approximate thickness of 5.5 mm and a stacking sequence according to $[45/0/-45/90]_{3S}$. The material is a combination of polyacrylonitrile (PAN) based carbon fibers in PYROFIL #360 resin which has a density of 1200 kg/m^3 and a glass transition temperature of $170 \text{ }^\circ\text{C}$ [68]. This resin is modified to allow curing in under 5 min, with a gel time of 200 sec at $130 \text{ }^\circ\text{C}$. The laminate is produced in an autoclave using compression molding for 7 min at $140 \text{ }^\circ\text{C}$ and a pressure of 8 MPa. The fiber volume fraction of the specimen is close to 60%. Finally, the specimen is cut to dimensions of 150 mm by 100 mm using a waterjet and conditioned to reduce the effect of moisture on the results.

3.1.2 Low-velocity impact

The ASTM D7136 test standard is considered for the impact testing [46]. A gravity-operated drop tower with a 7.72 kg impactor is used to perform the test. It drops the impactor from a height of 0.1 m onto the CFRP laminate, and prevents it from impacting again after the rebound. In the large-mass impact, the typical test durations are much longer than the required time for the stress waves to reach the boundaries [47]. The impactor is equipped with an Endevco Isotron 23-1 load cell holding a 16 mm diameter hemispherical hardened solid steel impact tip. It measures the compression force during the LVI. A line pattern is attached to the impactor to allow optical tracking of the vertical position using a Photron Fastcam SA-4 high-speed camera. The data acquisition is performed using an HBM GEN5i digital oscilloscope at a sampling rate of 1 MS/s. Based on the force signal, the oscilloscope sends a trigger signal to the camera to start recording the frames. The specimen temperature during the test is $29.74 \text{ }^\circ\text{C}$, which is recorded using a laser thermometer. The recorded force-displacement diagram is given in Figure 6, where the initial position before the impact is set at 0 mm. The actual impact energy was measured to be 5.3 J.

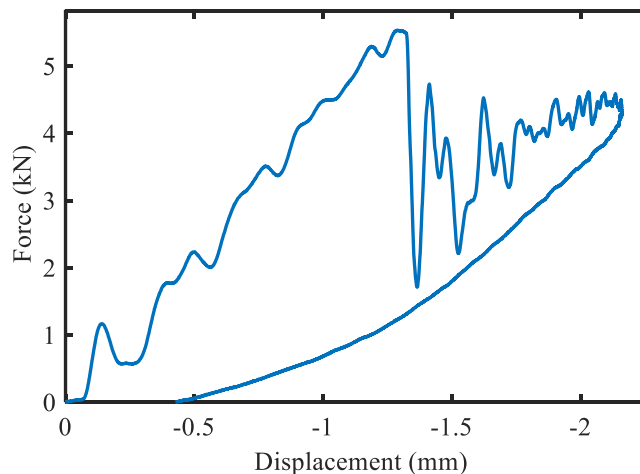


Figure 6: Force-displacement diagram of the LVI test from a height of 0.1 m on the CFRP laminate. The force is registered by the load cell and the displacement is obtained from the optical tracking.

3.2. Experimental methods

3.2.1 Ultrasonic testing

A spherically focused immersion transducer (Olympus V313) with a center frequency of 15 MHz is employed. This transducer is specifically chosen because of its broadband nature. The element diameter is 6.35 mm and the focal distance is 25.4 mm. The transducer is excited by an ultrasonic pulser/receiver (Tescan UTPR-CC-50) with a negative square wave. The voltage, capacity, and damping for the pulser are set at 150 V, 1070 pF, and 45 Ohm respectively. The signal is pre-amplified with a gain of 30 dB. The signal is then sampled by a 14-bit digitizer card (NI PXIe-5172) at a sampling rate of 250 MS/s. In total, 1300 time samples are stored for each A-scan signal. In order to increase the SNR, averaging has been

applied (16 averages per scan point). A 3-axis Cartesian scanner using a motion controller card (NI PXI-7350) is applied for raster scanning. The scan steps in both x and y directions are 0.2 mm and the scan area is 70 mm×70 mm (350×350 data points). The scan speeds in both x and y directions are set to 20 mm/s. The sample was rotated approximately 20° with respect to the scan coordinate system.

3.2.2 Optical microscopy

The impacted surface of the CFRP laminate has been investigated by a digital microscope (VHX-7000 Keyence) having a lens with a magnification factor of x200. A 3D stitching procedure is employed to image an area of 20mm x 25 mm in which the focus depth is dynamically adapted. This allows visualizing the 3D indentation profile, i.e. plastic deformation at the top surface, due to the impact event.

4. Results and discussions

The acquired ultrasonic pulse-echo data is processed in Matlab® R2019a. The computed A_{inst} and ϕ_{inst} of the ultrasonic response signals are displayed in Figure 7a and b respectively for two orthogonal planes at the center of the impact area.

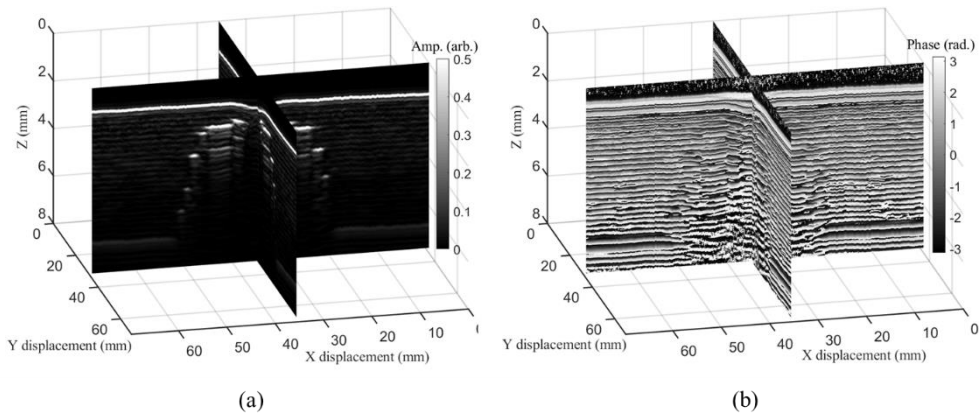


Figure 7: Orthogonal slices representing (a) the instantaneous amplitude and (b) the instantaneous phase of the recorded ultrasonic dataset.

4.1 STEP 1: Structural interfaces

Based on the analysis of the instantaneous amplitude (see section 2.1), the front-wall echo, back-wall echo, and delamination echo are extracted for each scanning instance. Figure 8a presents a projected visualization of the delamination cluster, clearly reflecting the quasi-isotropic stacking sequence of the impacted CFRP. The depth information of the damage can be obtained by multiplying the longitudinal sound speed in the thickness direction with the TOF between the front-wall echo and the delamination echoes. Figure 8b combines both the instantaneous amplitude and the depth information in order to obtain a 3D visualization of the internal delamination features due to the impact event. It can be readily seen that the impact-induced delamination cluster resembles a pine-tree pattern, which accords with earlier studies [48, 49]. Note that due to shadowing effects, overlapping delaminations cannot be imaged.

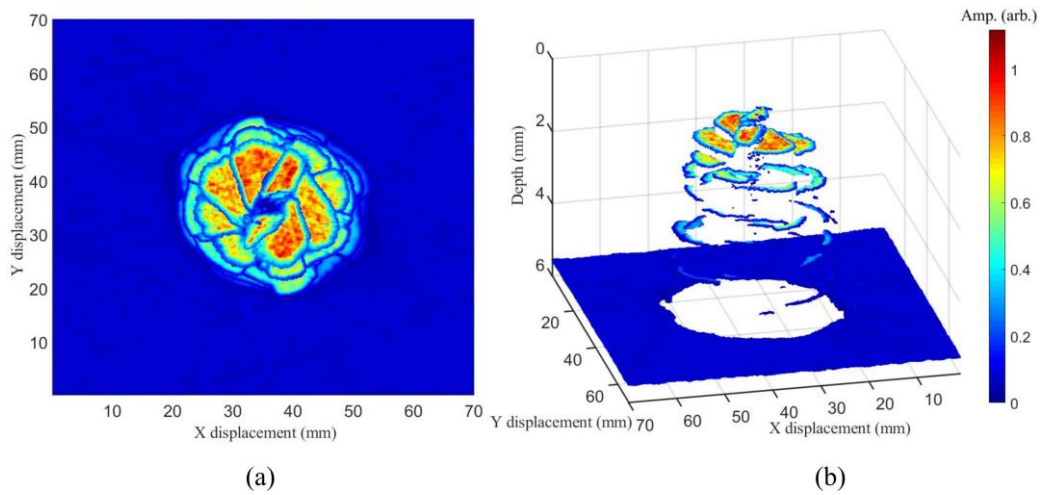


Figure 8: Visualization of barely visible impact damage: (a) top view and (b) 3D perspective view.

The hybrid instantaneous phase analysis introduced in section 2.1 is applied for extracting the interply tracks. The parameters of the applied Gabor filters are shown in the 1st and 2nd row of Table 1. The center frequency f_0 is determined based on the ply-resonance, the bandwidth σ_0 is chosen according to previous research [39]. The extracted positions of surfaces, delaminations, and interplies are superimposed on the instantaneous amplitude dataset in Figure 9. The global interply tracks appear quite continuous and smooth, resulting in nearly uniform-spaced positions of the interplies throughout the laminate. This indicates the high-quality manufacturing process of the CFRP laminate. Another interesting aspect of this hybrid instantaneous phase analysis is that information of the interplies near the delamination area is clearly provided. As such, the presumable crack path of progressive interply delamination is revealed which provides crucial information for damage evolution prognosis. Some local interply tracks show discontinuities, especially for the deep plies, which is due to the sensitivity of the instantaneous phase to noise features. Further, the ply tracks seem to be slightly distorted at specific (x,y) locations (see the orange indicators on Figure 9), which is likely related to slight warpage due to the manufacturing process. Also at the zone of impact, there seems to be a local distortion of the front surface and the sub-surface interply tracks. This will be discussed in a quantitative manner in the next section.

Table 1

The parameters of the applied log-Gabor filters

Function	f_0 (MHz)	σ_0	-6 dB bandwidth (MHz)
Fundamental ply-resonance	6	0.7	3.94 - 9.13
2nd-harmonic ply-resonance	12.5	0.8	9.61 - 16.26
Noise filtering	15	0.8	9.85 - 22.83

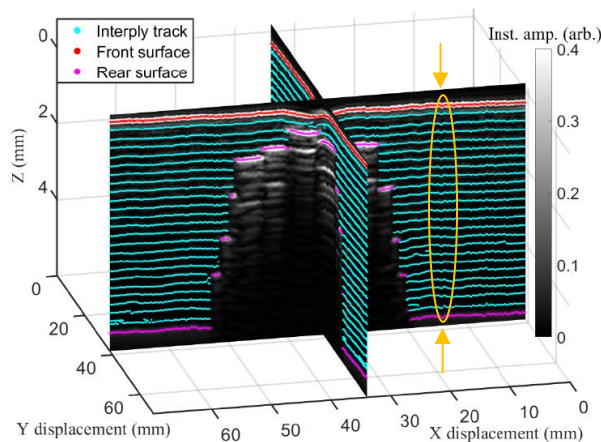


Figure 9: Orthographic projection slices through the instantaneous amplitude dataset. Superimposed are the front

surface (red lines), back surface and delaminations (magenta lines), and interply tracks (green lines) obtained by the hybrid analytic-signal analysis. The scaling is different in axes.

4. 2 STEP 2: Out-of-plane ply angles α

Out-of-plane features in the bulk of the CFRP sample are extracted by applying the structure tensor process (see section 2.2) to the instantaneous phase dataset. The instantaneous phase at the 2nd-harmonic ply-resonance is employed since it is close to the center frequency of the used transducer (high signal-to-noise ratio), and it is well-locked to the interply tracks. Figure 10 shows the measured out-of-plane ply angle map relative to the principal direction of the planar structure and the z-axis. The scan region away from the impact shows minor deviations from the nominal out-of-plane fiber angle of 0° , indicating the high manufacturing quality of the CFRP laminate. However, in certain areas slight warpages can be observed (see the orange indicators on Figure 10), having a typical angle of around $1-1.5^\circ$. This is in correspondence with the earlier observation in Figure 9.

Interestingly, Figure 10 clearly reveals an indent at the impact location due to local plasticity. The front-surface profile measured by optical microscopy is shown in Figure 11a. Note that the square patterns in the optical image are not material characteristics, but are attributed to the 3D stitching procedure in the microscopic imaging procedure. The front-surface profile is also extracted by the analysis of the ultrasonic front-wall echo (see Figure 11b). Both measurements indicate an indentation depth of $\sim 150 \mu\text{m}$. Figure 12 shows cross-sectional profiles through the indentation area, from which a consistent indentation geometry (width and depth) is observed. The benefit of the ultrasonic inspection is its capability to provide also information about the local plastic deformation inside the bulk of the CFRP laminate. It can be seen from Figure 10 that the plastic deformation is mainly concentrated in the top few plies directly beneath the impact location. Furthermore, the ultrasonic reconstruction indicates that small plastic deformation appears near the delamination edges. The limited plastic deformation may be attributed to the fact that the impact energy is mainly absorbed through the thickness direction of the laminate by ply splitting, and delamination formation [5]. The latter can be readily seen in Figure 8.

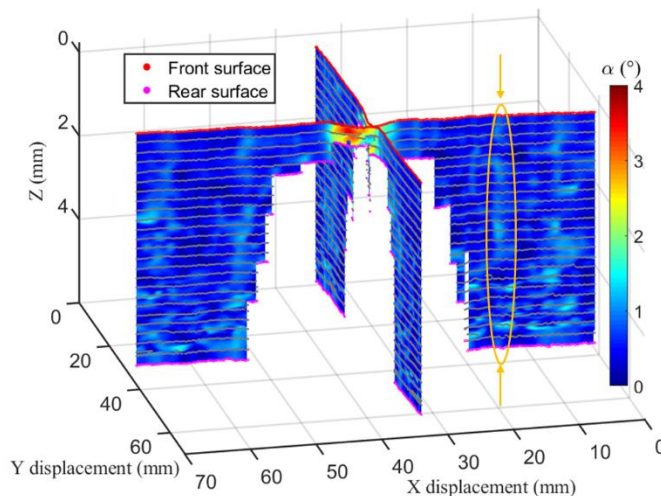


Figure 10: The reconstructed out-of-plane ply angle maps relative to the planar structure and the z-axis.

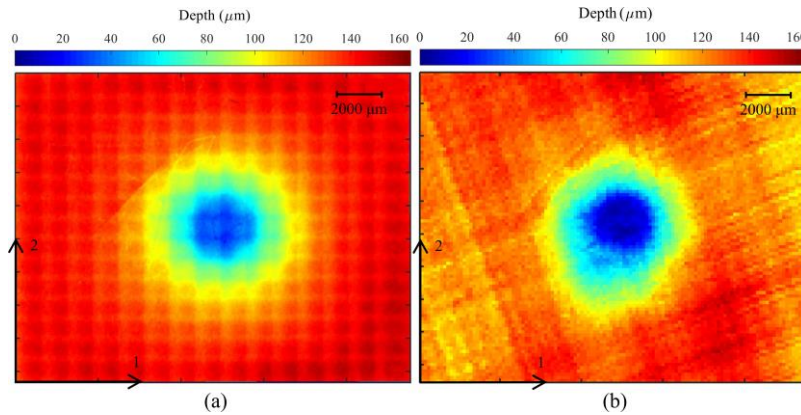


Figure 11: The measured front-surface profiles by (a) optical microscopy and (b) ultrasound.

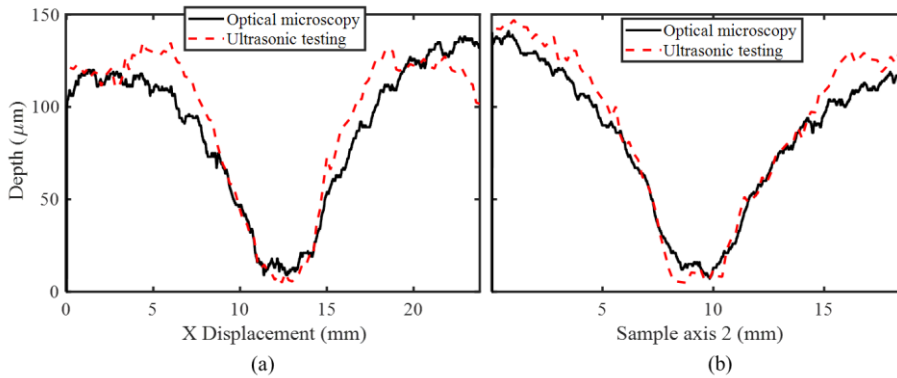


Figure 12: Cross-section through the impact position of the measured front-surface profiles along (a) sample axis 1 and (b) sample axis 2.

4. 3 STEP 3: In-plane fiber angles θ

The GF-ID method (see section 2.3) is applied to multiple slices of the instantaneous amplitude in view of extracting the in-plane fiber angles. This step 3 does not require the necessity to operate at the fundamental or the 2nd harmonic ply-resonance. Though, to improve the signal quality, a log-Gabor filter around the center frequency of the transducer is applied. The employed parameters are listed in the 3rd row of Table 1. The slices are taken such that they are parallel to the interply tracks extracted in section 4.1.

Figure 13a shows such a slice in the middle of the 7th ply, which has a nominal fiber angle of -45° . The 2D Gabor filter bank has wavelengths ranging from 4 to 16 pixels with a spacing of 1 pixel and angles ranging from 1° to 180° with a spacing of 1° . To avoid the presence of edge artifacts, a 2D Gabor filter surpassing an edge is not considered in the construction of the $ID_{x,y}(\theta, \lambda_s)$. The obtained scale map of the GF-ID procedure is presented in Figure 13b. More interesting for our application is the map of the identified local direction θ , see Figure 13c. Note that the angle of the scanning direction ($\sim 20^\circ$) has been compensated in the extraction of the in-plane fiber angles. For this specific slice, the results indicate an in-plane fiber angle of $\theta = -43.5^\circ \pm 7.0^\circ$ (mean \pm std) which is in good accordance with the nominal fiber angle for the 7th ply. Deviations from the nominal ply angle can be seen, especially near edge features.

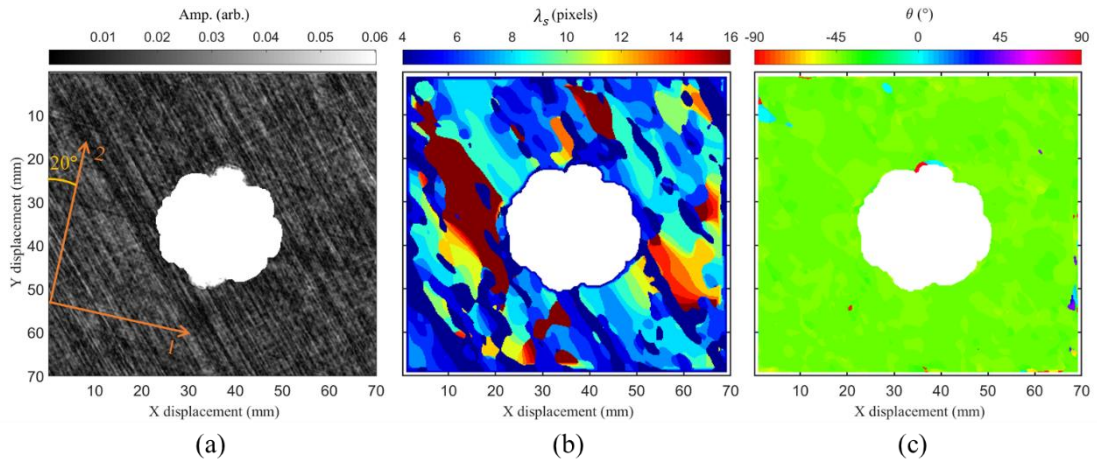


Figure 13: (a) Filtered instantaneous amplitude slice at the middle of the 7th ply (nominal angle of -45°); representation of the in-plane fiber (b) scale and (c) direction, reconstructed by the GF-ID method.

The procedure has been repeated for 120 slices through depth, and the obtained in-plane fiber directions are represented in Figure 14. The extracted global in-plane fiber directions correspond well to the nominal stacking sequence, i.e. $[45/0/-45/90]_{3S}$, of the studied CFRP laminate. However, the measured fiber direction in the 1st and the last plies shows many deviations due to the influence of the strong front- and back wall echoes. The significant ultrasonic attenuation for deep plies further complicates the stable extraction of the in-plane fiber angles θ .

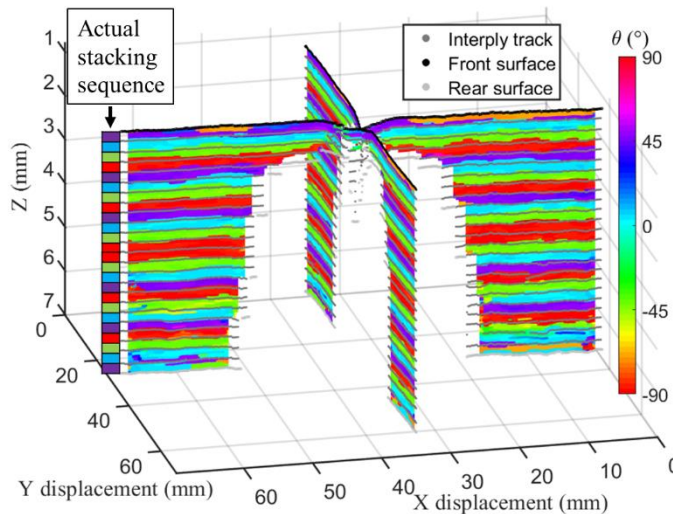


Figure 14: The reconstructed in-plane fiber angle maps by means of the GF-ID method. Superimposed in gray are the interply tracks. The actual stacking sequence is given as a reference.

5. Conclusion

An ultrasonic pulse-echo method, coupled to tomographic reconstruction approaches, has been proposed to extract both damage features and the local ply-fiber architecture of composites. This so-called planar ultrasound computed tomography (pU-CT) technique relies on the use of ply-resonances, and involves 3 main analysis steps:

- Step 1: Mapping ply-interfaces via a hybrid analytic-signal analysis;
- Step 2: Reconstructing the local out-of-plane ply orientation via a structure tensor process;
- Step 3: Extracting the local in-plane fiber direction via a Gabor Filter-based Information Diagram GF-ID.

The proposed pU-CT method has been applied on a 5.5 mm thick CFRP laminate with a stacking sequence $[45/0/-45/90]_{3S}$. The 24-layer CFRP laminate suffered a low-velocity impact of 5.3 J, resulting in barely visible impact damage. The impact event induced local plasticity, resulting in an indentation profile at the impact location. The indentation profile measured by pU-CT has been validated by 3D optical microscopy. Further, the pU-CT results clearly show the presence of sub-surface plastic deformation, resulting in out-of-plane ply wrinkling. This local plasticity is mainly limited to the first few plies beneath the impact location. The pU-CT also provided a view on the complex delamination cluster which spreads throughout the depth of the CFRP laminate. The detailed reconstruction of the ply tracks near the delamination edges provides a means to predict the presumable crack propagation path during damage evolution. The reconstructed in-plane fiber angles remained unaffected by the impact event, and closely matched the nominal quasi-isotropic stacking sequence of the manufactured CFRP laminate.

The proposed pU-CT seems to offer a complementary methodology to X-CT for reconstructing the local fiber architecture and complex damage phenomena in CFRP laminates.

6. Acknowledgment

This work is supported by China Scholarship Council and Ghent University Preference CSC program (No. 01SC0219), Bijzonder Onderzoeksfonds Ghent University (BOF 01N01719), and the National Natural Science Foundation of China (No. U1709206).

Reference

- [1] Barile, C., Casavola, C., and De Cillis, F., 2019, "Mechanical comparison of new composite materials for aerospace applications," *Composites Part B: Engineering*, 162, pp. 122-128.
- [2] Amann, C., Kreissl, S., Grass, H., and Meinhardt, J., 2017, "A review on process-induced distortions of carbon fiber reinforced thermosets for large-scale production," *Prod Eng-Res Dev*, 11(6), pp. 665-675.
- [3] Sohn, M., Hu, X., Kim, J. K., and Walker, L., 2000, "Impact damage characterisation of carbon fibre/epoxy composites with multi-layer reinforcement," *Composites Part B: Engineering*, 31(8), pp. 681-691.
- [4] Azouaoui, K., Azari, Z., and Pluvinage, G., 2010, "Evaluation of impact fatigue damage in glass/epoxy composite laminate," *International journal of Fatigue*, 32(2), pp. 443-452.
- [5] Chen, D., Luo, Q., Meng, M., Li, Q., and Sun, G., 2019, "Low velocity impact behavior of interlayer hybrid composite laminates with carbon/glass/basalt fibres," *Composites Part B: Engineering*, 176, p. 107191.
- [6] Karakuzu, R., Erbil, E., and Aktas, M., 2010, "Impact characterization of glass/epoxy composite plates: An experimental and numerical study," *Composites Part B: Engineering*, 41(5), pp. 388-395.
- [7] Liv, Y., Guillaumet, G., Costa, J., González, E., Marín, L., and Mayugo, J., 2017, "Experimental study into compression after impact strength of laminates with conventional and nonconventional ply orientations," *Composites Part B: Engineering*, 126, pp. 133-142.
- [8] Daelemans, L., Cohades, A., Meireman, T., Beckx, J., Spronk, S., Kersemans, M., De Baere, I., Rahier, H., Michaud, V., Van Paepegem, W., and De Clerck, K., 2018, "Electrospun nanofibrous interleaves for improved low velocity impact resistance of glass fibre reinforced composite laminates," *Mater Design*, 141, pp. 170-184.
- [9] Gonzalez, E. V., Maimi, P., Camanho, P. P., Lopes, C. S., and Blanco, N., 2011, "Effects of ply clustering in laminated composite plates under low-velocity impact loading," *Compos Sci Technol*, 71(6), pp. 805-817.
- [10] Vieille, B., Casado, V. M., and Bouvet, C., 2014, "Influence of matrix toughness and ductility on the compression-after-impact behavior of woven-ply thermoplastic- and thermosetting-composites: A comparative study," *Compos Struct*, 110, pp. 207-218.
- [11] Dilonardo, E., Nacucchi, M., De Pascalis, F., Zarrelli, M., and Giannini, C., 2020, "High resolution X-ray computed tomography: A versatile non-destructive tool to characterize CFRP-based aircraft composite elements," *Compos Sci Technol*, 192, p. 108093.
- [12] Gao, J., Kadir, N., Kirk, C. D., Hernandez, J., Wang, J., Paulson, S., Zhai, X., Horn, T., Kim, G., and Gao, J., 2021, "Real-time damage characterization for GFRCs using high-speed synchrotron X-ray phase contrast imaging," *Composites Part B: Engineering*, 207, p. 108565.
- [13] Garcea, S., Wang, Y., and Withers, P., 2018, "X-ray computed tomography of polymer composites," *Compos Sci Technol*, 156, pp. 305-319.
- [14] Prade, F., Schaff, F., Senck, S., Meyer, P., Mohr, J., Kastner, J., and Pfeiffer, F., 2017, "Non-destructive

characterization of fiber orientation in short fiber reinforced polymer composites with X-ray vector radiography," *Ndt&E Int*, 86, pp. 65-72.

- [15] Tan, K. T., Watanabe, N., and Iwahori, Y., 2011, "X-ray radiography and micro-computed tomography examination of damage characteristics in stitched composites subjected to impact loading," *Composites Part B: Engineering*, 42(4), pp. 874-884.
- [16] Straumit, I., Lomov, S. V., and Wevers, M., 2015, "Quantification of the internal structure and automatic generation of voxel models of textile composites from X-ray computed tomography data," *Compos Part a-Appl S*, 69, pp. 150-158.
- [17] Wan, Y., Straumit, I., Takahashi, J., and Lomov, S. V., 2016, "Micro-CT analysis of internal geometry of chopped carbon fiber tapes reinforced thermoplastics," *Compos Part a-Appl S*, 91, pp. 211-221.
- [18] Allevato, G., Hinrichs, J., Rutsch, M., Adler, J., Jäger, A., Pesavento, M., and Kupnik, M., 2020, "Real-time 3D imaging using an air-coupled ultrasonic phased-array," *IEEE Transactions on Ultrasonics, Ferroelectrics, and Frequency Control*.
- [19] Blandford, B. M., and Jack, D. A., 2020, "High resolution depth and area measurements of low velocity impact damage in carbon fiber laminates via an ultrasonic technique," *Composites Part B: Engineering*, 188, p. 107843.
- [20] Caminero, M., García-Moreno, I., and Rodríguez, G., 2018, "Experimental study of the influence of thickness and ply-stacking sequence on the compression after impact strength of carbon fibre reinforced epoxy laminates," *Polymer Testing*, 66, pp. 360-370.
- [21] Ingram, M., Mineo, C., Gachagan, A., Mulholland, A. J., Nordon, A., and Hegarty, M., 2020, "Determination of bubble size distribution using ultrasound array imaging," *IEEE transactions on ultrasonics, ferroelectrics, and frequency control*, 67(7), pp. 1424-1437.
- [22] Katunin, A., Wronkiewicz-Katunin, A., and Dragan, K., 2020, "Impact damage evaluation in composite structures based on fusion of results of ultrasonic testing and X-ray computed tomography," *Sensors-Basel*, 20(7), p. 1867.
- [23] Marcantonio, V., Monarca, D., Colantoni, A., and Cecchini, M., 2019, "Ultrasonic waves for materials evaluation in fatigue, thermal and corrosion damage: A review," *Mech Syst Signal Pr*, 120, pp. 32-42.
- [24] Morokov, E., Levin, V., Chernov, A., and Shanygin, A., 2021, "High resolution ply-by-ply ultrasound imaging of impact damage in thick CFRP laminates by high-frequency acoustic microscopy," *Compos Struct*, 256, p. 113102.
- [25] Pelivanov, I., Ambroziński, Ł., Khomenko, A., Koricho, E. G., Cloud, G. L., Haq, M., and O'Donnell, M., 2016, "High resolution imaging of impacted CFRP composites with a fiber-optic laser-ultrasound scanner," *Photoacoustics*, 4(2), pp. 55-64.
- [26] Růžek, R., Lohonka, R., and Jironč, J., 2006, "Ultrasonic C-Scan and shearography NDI techniques evaluation of impact defects identification," *Ndt&E Int*, 39(2), pp. 132-142.
- [27] Li, C., Pain, D., Wilcox, P. D., and Drinkwater, B. W., 2013, "Imaging composite material using ultrasonic arrays," *Ndt&E Int*, 53, pp. 8-17.
- [28] Ciampa, F., Mahmoodi, P., Pinto, F., and Meo, M., 2018, "Recent advances in active infrared thermography for non-destructive testing of aerospace components," *Sensors-Basel*, 18(2), p. 609.
- [29] Hedayatrasa, S., Poelman, G., Segers, J., Van Paepegem, W., and Kersemans, M., 2019, "Performance of frequency and/or phase modulated excitation waveforms for optical infrared thermography of CFRPs through thermal wave radar: A simulation study," *Compos Struct*, 225, p. 111177.
- [30] Meola, C., Boccardi, S., Carlomagno, G., Boffa, N., Ricci, F., Simeoli, G., and Russo, P., 2017, "Impact damaging of composites through online monitoring and non-destructive evaluation with infrared thermography," *Ndt&E Int*, 85, pp. 34-42.
- [31] Towsyfyhan, H., Biguri, A., Boardman, R., and Blumensath, T., 2020, "Successes and challenges in non-destructive testing of aircraft composite structures," *Chinese Journal of Aeronautics*, 33(3), pp. 771-791.
- [32] Wang, F., Liu, J. Y., Liu, Y., and Wang, Y., 2016, "Research on the fiber lay-up orientation detection of unidirectional CFRP laminates composite using thermal-wave radar imaging," *Ndt&E Int*, 84, pp. 54-66.
- [33] Cheng, J., Qiu, J., Ji, H., Wang, E., Takagi, T., and Uchimoto, T., 2017, "Application of low frequency ECT method in noncontact detection and visualization of CFRP material," *Composites Part B: Engineering*, 110, pp. 141-152.
- [34] Huang, S., and Wang, S., 2016, *New technologies in electromagnetic non-destructive testing*, Springer.
- [35] Mizukami, K., Mizutani, Y., Todoroki, A., and Suzuki, Y., 2016, "Detection of in-plane and out-of-plane fiber waviness in unidirectional carbon fiber reinforced composites using eddy current testing," *Composites Part B: Engineering*, 86, pp. 84-94.
- [36] Song, H., and Yang, Y., 2020, "Super-resolution visualization of subwavelength defects via deep learning-enhanced ultrasonic beamforming: A proof-of-principle study," *Ndt&E Int*, 116, p. 102344.
- [37] Smith, R. A., Nelson, L. J., Mienczakowski, M. J., and Wilcox, P. D., 2017, "Ultrasonic analytic-signal responses from

- polymer-matrix composite laminates," *IEEE transactions on ultrasonics, ferroelectrics, and frequency control*, 65(2), pp. 231-243.
- [38] Yang, X., Verboven, E., Ju, B.-f., and Kersemans, M., 2021, "Comparative study of ultrasonic techniques for reconstructing the multilayer structure of composites," *Ndt&E Int*, p. 102460.
- [39] Yang, X., Verboven, E., Ju, B.-f., and Kersemans, M., 2021, "Parametric study on interply tracking in multilayer composites by analytic-signal technology," *Ultrasonics*, 111, p. 106315.
- [40] Nelson, L., and Smith, R., 2019, "Fibre direction and stacking sequence measurement in carbon fibre composites using Radon transforms of ultrasonic data," *Composites Part A: Applied Science and Manufacturing*, 118, pp. 1-8.
- [41] Larrañaga-Valsero, B., Smith, R. A., Tayong, R. B., Fernández-López, A., and Güemes, A., 2018, "Wrinkle measurement in glass-carbon hybrid laminates comparing ultrasonic techniques: A case study," *Composites Part A: Applied Science and Manufacturing*, 114, pp. 225-240.
- [42] Nelson, L., Smith, R., and Mienczakowski, M., 2018, "Ply-orientation measurements in composites using structure-tensor analysis of volumetric ultrasonic data," *Composites Part A: Applied Science and Manufacturing*, 104, pp. 108-119.
- [43] Pinter, P., Dietrich, S., Bertram, B., Kehrer, L., Elsner, P., and Weidenmann, K. A., 2018, "Comparison and error estimation of 3D fibre orientation analysis of computed tomography image data for fibre reinforced composites," *Ndt&E Int*, 95, pp. 26-35.
- [44] Kruizinga, P., and Petkov, N., 1999, "Nonlinear operator for oriented texture," *IEEE Transactions on image processing*, 8(10), pp. 1395-1407.
- [45] Kamarainen, J., Kyrki, V., and Kalviainen, H., "Fundamental frequency Gabor filters for object recognition," *Proc. Object recognition supported by user interaction for service robots*, IEEE, pp. 628-631.
- [46] Standard, A., 2015, "D7136/D7136M-15, Standard Test Method for Measuring the Damage Resistance of a Fiber-Reinforced Polymer Matrix Composite to a Drop-Weight Impact Event," *ASTM International*, West Conshohocken, PA.
- [47] Spronk, S., Kersemans, M., De Baerdemaeker, J., Gilabert, F., Sevenois, R., Garoz, D., Kassapoglou, C., and Van Paepegem, W., 2018, "Comparing damage from low-velocity impact and quasi-static indentation in automotive carbon/epoxy and glass/polyamide-6 laminates," *Polymer Testing*, 65, pp. 231-241.
- [48] Balakrishnan, V. S., Wartig, K., Tsombanis, N., and Seidlitz, H., 2019, "Influence of processing parameters on the impact behaviour of glass/polyamide-6 composite," *Composites Part B: Engineering*, 159, pp. 292-299.
- [49] De Freitas, M., Silva, A., and Reis, L., 2000, "Numerical evaluation of failure mechanisms on composite specimens subjected to impact loading," *Composites Part B: Engineering*, 31(3), pp. 199-207.